

Shear Flow Generation and Energetics in Electromagnetic Turbulence

V. Naulin, A. Kendl*, O. E. Garcia, A. H. Nielsen, and J. Juul Rasmussen

Association EURATOM-Risø National Laboratory,

OPL-128 Risø, DK-4000 Roskilde, Denmark and

**) University of Innsbruck, Institute for Theoretical Physics,*

Association EURATOM-ÖAW, A-6020 Innsbruck, Austria

(Dated: July 9, 2018)

Abstract

Zonal flows are recognised to play a crucial role for magnetised plasma confinement. The genesis of these flows out of turbulent fluctuations is therefore of significant interest. We investigate the relative importance of zonal flow generation mechanisms via the Reynolds stress, Maxwell stress, and geodesic acoustic mode (GAM) transfer in drift-Alfvén turbulence. By means of numerical computations we quantify the energy transfer into zonal flows owing to each of these effects. The importance of the three driving ingredients in electrostatic and electromagnetic turbulence for conditions relevant to the edge of fusion devices is revealed for a broad range of parameters. The Reynolds stress is found to provide a flow drive, while the electromagnetic Maxwell stress is in the cases considered a sink for the flow energy. In the limit of high plasma beta, where electromagnetic effects and Alfvén dynamics are important, the Maxwell stress is found to cancel the Reynolds stress to a high degree. The geodesic oscillations, related to equilibrium pressure profile modifications due to poloidally asymmetric transport, can act as both sinks as drive terms, depending on the parameter regime. For high beta cases the GAMs are the main drive of the flow. This is also reflected in the frequency dependence of the flow, showing a distinct peak at the GAM frequency in that regime.

PACS numbers: 52.25.Gj, 52.35.Ra, 52.65.Kj

I. INTRODUCTION

Since the discovery of the H-mode [1] in magnetically confined plasmas a multitude of mechanisms for the generation of the shear flow connected to the LH-transition have been proposed. They include amongst others ion-orbit loss effects, neoclassical effects, and turbulent flow generation [2, 3, 4]. Here we focus on turbulence as a source of shear flow generation. It was already early recognized that turbulence can lead to spontaneous self-organization of turbulent energy into sheared poloidal flows which in turn could reduce the transport significantly [5]. A conclusive computational demonstration of shear flow generation by turbulence in realistic geometry of fusion devices, which is sufficient for achievement of the LH-transition, has, however, not yet been achieved. In electrostatic turbulence the Reynolds stress is the main source of interaction between large scale flows and small scale turbulence. The Reynolds stress designates the radial flux of poloidal momentum, and a finite radial gradient of it will be an indication for a local condensation of momentum into a poloidal flow. In electromagnetic turbulence an additional source of poloidal flow generation has to be accounted for: the Maxwell stress, which arises from parallel momentum transport along perturbed magnetic field lines. Measurements of the Reynolds stress and its radial variation have been performed in several fusion devices with the purpose to identify it as a source of sheared poloidal rotation [6]. Recently, also the Maxwell stress, respectively, magnetic fluctuations and their cross-correlations have been measured in Reversed Field Pinch (RFP) [7] and Tokamak [8] configurations. These measurements indicate that the Maxwell stress acts as a sink for poloidal flow energy. Finally, in the presence of toroidal magnetic field inhomogeneity the geodesic acoustic modes (GAMs) [9] interact with the poloidal flows in the system. In such cases the zonal flows show a residual oscillation at the GAM frequency.

The purpose of this paper is to investigate these three different transfer mechanisms for zonal flow generation over a wide range of parameters as neither their strength nor their detailed (driving or damping) effect on the flows are a priori sufficiently clear. While the Reynolds stress is most often identified as a flow drive, there is considerable confusion about the role of the GAMs [10, 11]. The Maxwell stress is in low β situations rather weak, but it has been found to drain energy from the flow [12] and in high β situations it should ideally cancel the Reynolds stress [13].

This paper is organized as follows: In the following Section II we present the turbulence model used for the computations. The next Section III is devoted to discussion of the various transfer mechanisms of energy between turbulence and flow motion in a low and a high beta case. We then

present global scalings of the transfer terms with collisionality and plasma beta in Sec. IV. Finally we discuss our results in the concluding section.

II. ELECTROMAGNETIC TURBULENCE MODEL

We investigate the detailed balance of drive and sink terms for global poloidal flows in a model for plasma turbulence in the edge region of magnetic confinement devices. Considering both electrostatic and electromagnetic effects, together with toroidal geometry and magnetic field curvature in a flux tube model, allows us to investigate the different turbulent momentum transfer terms responsible for flow generation.

The fluid equations for drift-Alfvén turbulence in 3-dimensional flux tube geometry result from standard ordering based upon the slowness of the dynamics compared to the ion gyro frequency $\Omega_i = eB/M_i$ and the smallness of the drift scale ρ_s compared to the background pressure gradient scale length L_\perp . These quantities and the sound speed c_s are defined by

$$\Omega_i = \frac{eB}{M_i}, \quad c_s^2 = \frac{T_e}{M_i}, \quad \rho_s = \frac{c_s}{\Omega_i}, \quad L_\perp = |\nabla \log p_e|^{-1}, \quad (1)$$

where subscripts e, i refer to electrons or ions respectively, and the temperature is given in units of energy. Normalization is in terms of scaled dependent variables (electrostatic potential $e\phi/T_e$, electron density n/n_{00} , parallel ion velocity u/c_s , parallel electric current $J/n_{00}ec_s$). In addition the dependent quantities are scaled with the small drift parameter $\delta = \rho_s/L_\perp$, so that mainly terms of order one appear in the normalised set of equations.

The scale perpendicular to the magnetic field is in units of ρ_s ; the parallel scale is $L_\parallel = qR$, with R the toroidal major radius and q the safety factor and the closed flux surface connection length $2\pi L_\parallel$. The time scale is L_\perp/c_s . Further details for this system and geometry are given in Ref. [14]. In the present paper we use a constant background temperature for electrons, and assume cold ions. The quantity n_{00} is a normalizing density, while $n_0(x)$ is the equilibrium plasma density having a finite gradient. In normalized units the radial profile of the density is $\partial_x \log n_0(x) = -1$. Thus x serves as the radial coordinate. Relative to the background magnetic field \vec{B} the other perpendicular coordinate is y . Finally the parallel coordinate is denoted by z .

As singly charged ions and quasi-neutral dynamics are assumed, n_0 and n refer to both the electron and ion density. It is important to note that n_0 and n equivalently describe electron density or pressure; we neglect temperature dynamics in this qualitative study because of the similarity in

physical character between the electron temperature and the “non-adiabatic” part of the electron density [15]. The model is described by the temporal evolution of the electrostatic potential (ϕ), density perturbations (n), parallel current (J), and parallel ion velocity (u). Auxiliary variables are the vorticity (Ω) and the parallel component of the magnetic vector potential (A_{\parallel}):

$$\frac{\partial \Omega}{\partial t} + \vec{v}_E \cdot \nabla \Omega = \mathcal{K}(n) + \nabla_{\parallel} J + \mu_{\Omega} \nabla_{\perp}^2 \Omega, \quad (2)$$

$$\frac{\partial n}{\partial t} + \vec{v}_E \cdot \nabla (n_0 + n) = \mathcal{K}(n - \phi) + \nabla_{\parallel} (J - u) + \mu_n \nabla_{\perp}^2 n, \quad (3)$$

$$\frac{\partial}{\partial t} (\hat{\beta} A_{\parallel} + \hat{\mu} J) + \hat{\mu} \vec{v}_E \cdot \nabla J = \nabla_{\parallel} (n_0 + n - \phi) - C J, \quad (4)$$

$$\hat{\varepsilon} \left(\frac{\partial u}{\partial t} + \vec{v}_E \cdot \nabla u \right) = -\nabla_{\parallel} (n_0 + n), \quad (5)$$

with the vorticity Ω and current (Ampere’s law) J given by

$$\Omega = \nabla_{\perp}^2 \phi, \quad J = -\nabla_{\perp}^2 A_{\parallel}. \quad (6)$$

The advective and parallel derivatives carry non-linearities entering through ϕ and A_{\parallel} , which – due to the description of the geometry – can be expressed in terms of a Poisson bracket

$$\{f, g\} = \frac{\partial f}{\partial x} \frac{\partial g}{\partial y} - \frac{\partial f}{\partial y} \frac{\partial g}{\partial x} \quad (7)$$

in the xy -plane as

$$\vec{v}_E \cdot \nabla = \{\phi, \cdot\}; \quad \nabla_{\parallel} = \frac{\partial}{\partial z} - \{\hat{\beta} A_{\parallel}, \cdot\}. \quad (8)$$

The curvature operator \mathcal{K} is for simple circular toroidal geometry written as

$$\mathcal{K} = -\omega_B \left(\sin z \frac{\partial}{\partial x} + \cos z \frac{\partial}{\partial y} \right), \quad (9)$$

and originates from compressibility terms of the form $\nabla \cdot (1/B^2) \vec{B} \times \nabla$. Note that z takes values in the range $[-\pi : \pi]$ and that the outboard mid-plane is located at $z = 0$. The perpendicular Laplacian is in the locally shifted metric [14] written as

$$\nabla_{\perp}^2 = \left(\frac{\partial^2}{\partial x^2} + \frac{\partial^2}{\partial y^2} \right), \quad (10)$$

and is due to $-\nabla \cdot (B^{-2} \vec{B} \times \vec{B} \times \nabla)$, thus hiding magnetic shear in the shifting procedure. The viscous/diffusive terms $\sim \mu_{\Omega}, \mu_n$ in Eqs. (2) and (3) are introduced to provide sub-grid dissipation

of small scale dynamics.

The parameters in the equations reflect the competition between parallel and perpendicular dynamics, governed by the scale ratio $\hat{\epsilon} = (qR/L_\perp)^2$. The electron parallel dynamics is controlled by

$$\hat{\beta} = \frac{2\mu_0 p_e}{B^2} \hat{\epsilon}, \quad \hat{\mu} = \frac{m_e}{M_i} \hat{\epsilon}, \quad C = 0.51 \frac{L_\perp}{\tau_e c_s} \hat{\mu} = \hat{v} \hat{\mu}, \quad (11)$$

where τ_e is the electron collision time and the factor 0.51 reflects the parallel resistivity [16]. The competition between these three parameters, representing magnetic induction, electron inertia, and resistive relaxation, determines the response of J to the static force imbalance in Eq. (4). Due to the presence of ∇_\perp^2 in Eq. (6) this adiabatic response has different character in different parts of the spectrum. The last physical parameter is ω_B in Eq. (9), reflecting the effects of magnetic curvature (equivalently magnetic gradient, in a toroidal model). An important note is that all magnetic induction $\partial A_\parallel / \partial t$ and flutter $\hat{\beta}\{A_\parallel, \cdot\}$ effects enter through the finite beta $\beta = 2\mu_0 p_e / B^2$ or c_s^2 / v_A^2 , where v_A is the Alfvén velocity, and $\hat{\beta} = \beta_e \hat{\epsilon}$.

The density equation is augmented by damping layers in the left and right 5% of the radial domain, regulating the poloidally averaged density, e.g. the profile modification, back to zero. This feedback control of the profile arranges for the average density profile to stay close to the one characterized by the originally defined gradient.

III. ENERGETICS AND EVOLUTION OF FLOWS

The equation determining the evolution of zonal flows is found from the vorticity equation Eq. (2) by averaging over a flux surface as

$$\frac{\partial V_0}{\partial t} + \frac{\partial}{\partial x} \langle v_x v_y \rangle - \hat{\beta} \frac{\partial}{\partial x} \langle B_x B_y \rangle + \omega_B \langle n \sin z \rangle = \mu_\Omega \frac{\partial^2 V_0}{\partial x^2}, \quad (12)$$

where $\langle \cdot \rangle = (1/2\pi L_y) \int_{-\pi}^{\pi} dz \int_0^{L_y} dy \cdot$ denotes the flux surface average. The $E \times B$ velocity is given by $\mathbf{v}_E = (v_x, v_y, 0) = (-\partial_y \phi, \partial_x \phi, 0)$ and the electric field connected to the poloidal flow is described by the potential $\Phi_0(x) = \langle \phi \rangle$.

Consequently $V_0(x) = \langle v_y \rangle = \partial_x \Phi_0$ and $\langle \Omega \rangle = \partial_x V_0$. The first contribution to the flow evolution is the Reynolds stress, which is the radial transport of poloidal momentum by radial velocity fluctuations. It demands a correlation between the two components of the fluctuating velocity, which may be due to a seed flow or a background gradient, as is the case here. The second contribution arises from magnetic flutter. It can be interpreted as parallel current flowing radially along

perturbed magnetic field lines. The third term is the acceleration of the flow due to interaction with density sidebands via the compressibility of the diamagnetic drift, associated with geodesic acoustic modes. Finally, viscosity on the right hand side of Eq. 12 introduces a damping of the flow profile.

We are interested in the energetics of the flow evolution. To find the evolution of the energy in the mean flow we multiply the vorticity equation Eq. (2) by the flow velocity and integrate over the whole volume. We then obtain for the time evolution of the mean flow energy $U := (1/2) \int d\mathbf{x} V_0^2$:

$$\frac{dU}{dt} = \mathcal{R} + \mathcal{M} + \mathcal{G} + \mathcal{V}, \quad (13)$$

with the quantities \mathcal{R} , \mathcal{M} , \mathcal{G} , and \mathcal{V} defined as follows: From the convection we find

$$\mathcal{R} = \int d\mathbf{x} \Phi_0 \langle \mathbf{v}_E \cdot \nabla_{\perp} \Omega \rangle = \int d\mathbf{x} \langle v_x v_y \rangle \partial_x V_0, \quad (14)$$

which is the Reynolds stress contribution to the flow drive. Correspondingly the parallel current and magnetic fluctuations lead to

$$\mathcal{M} = \int d\mathbf{x} \Phi_0 \langle \nabla_{\parallel} J \rangle = -\hat{\beta} \int d\mathbf{x} \langle B_x B_y \rangle \partial_x V_0, \quad (15)$$

which is the Maxwell stress governing the energy exchange of the flow with magnetic fluctuations, where $B_x = \partial_y A_{\parallel}$ and $B_y = -\partial_x A_{\parallel}$. While the contribution of the normal curvature vanishes, the geodesic curvature results in a term associated with the geodesic acoustic modes (GAMs):

$$\mathcal{G} = \int d\mathbf{x} \Phi_0 \langle \omega_B \sin s \partial_x n \rangle = -\omega_B \int d\mathbf{x} \langle n V_0 \sin s \rangle. \quad (16)$$

The collisional damping finally is always a sink:

$$\mathcal{V} = -\mu_{\Omega} \int d\mathbf{x} \Phi_0 \langle \nabla_{\perp}^2 \Omega \rangle = -\mu_{\Omega} \int d\mathbf{x} (\partial_x V_0)^2. \quad (17)$$

Flow generation by Reynolds stresses is well known to result from an average phase correlation between the velocity fluctuations in the drift plane spanned by the x and y coordinate axes. The tendency of convective structures to be tilted with a seed sheared flow makes the transfer term \mathcal{R} generally positive, draining energy from the fluctuating motions to the zonal flows [17].

It is worthwhile to note that in pure MHD turbulence there is an approximate balance between Maxwell and Reynolds stress [13]. From a local linear analysis of modes, neglecting the toroidicity of the equilibrium magnetic field, we obtain the following functional relationship between the

fluctuations in magnetic potential and electrostatic potential:

$$A_{\parallel} = \frac{(\omega_B k_y)/(k_{\parallel} k_{\perp}^2) + c}{[\omega_B k_y c(\hat{\beta} - \hat{\mu} k_{\perp}^2)]/[k_{\parallel} k_{\perp}^2] + 1} \phi, \quad (18)$$

with $c = \omega/k_{\parallel}$. The dispersion relation has several branches (see Scott [18]). In the limit of high $\hat{\beta}$ and neglecting effects of curvature, the Alfvén branch of the dispersion relation dominates and c can be approximated by the Alfvén speed $v_A = \hat{\beta}^{-1/2}$:

$$A_{\parallel} = \phi/\sqrt{\hat{\beta}}. \quad (19)$$

As a consequence the Maxwell and Reynolds stress cancel in that regime, which is expressing the fact that Alfvén waves do not transport poloidal momentum.

From the plasma continuity equation (3) we find the evolution of the density sidebands,

$$\frac{\partial}{\partial t} \langle n \sin z \rangle + \frac{\partial}{\partial x} \langle \sin z n \frac{\partial \phi}{\partial y} \rangle + \omega_B \langle \sin^2 z \frac{\partial n}{\partial x} \rangle = \omega_B \langle \sin^2 z \frac{\partial \phi}{\partial x} \rangle - \langle \sin z \frac{\partial u}{\partial z} \rangle. \quad (20)$$

The contribution from the flow $V_0 = \partial\phi_0/\partial x$ in the first term on the right hand side of Eq. (20), describing the up-down asymmetric plasma compression due to poloidal rotation, couples with the zonal flow equation (12) and results in geodesic acoustic modes (GAMs) at frequency $\omega_B/\sqrt{2}$ (Refs. [9, 10, 19, 20]). Other terms in Eq. (20), along with coupling to the ion flow sidebands, may cause an acceleration of zonal flows in the presence of poloidally asymmetric particle fluxes, known as Stringer-Winsor spin-up [10, 19, 20, 21]. In this connection we also note that the energy transfer due to toroidal geometry into the energy of the fluctuating motions

$$\mathcal{K} = \frac{1}{2} \int d\mathbf{x} \tilde{v}^2, \quad (21)$$

is given by

$$- \int d\mathbf{x} \tilde{\phi} \mathcal{K}(n) = -\omega_B \int d\mathbf{x} \left(\sin s n \frac{\partial \phi}{\partial x} + \cos s n \frac{\partial \phi}{\partial y} \right).$$

This indeed indicates the tendency towards a ballooning structure of the fluctuations, since this term drives velocity fluctuations when the turbulent plasma transport is radially outwards from the torus axis and poloidally towards the out-board mid-plane. This geodesic transfer process was recently revisited in Ref. [11], where it was claimed that the GAM transfer is generally from the zonal flows through the density side-bands to the turbulent fluctuations.

IV. STRUCTURE OF ELECTROMAGNETIC FLUCTUATIONS

To address the simultaneous action of the energetic transfer effects we resort to three-dimensional numerical computations of the four-field model eqs. (2)- (5) on a grid of usually $64 \times 256 \times 32$ points, with dimensions $64 \times 256 \times 2\pi$ in x , y and z , respectively. Some runs were repeated at higher resolution $128 \times 512 \times 32$ to ensure convergence. The numerical scheme uses a symmetry, energy and vorticity conserving discretisation of the bracket structure of the nonlinearities [22] with the curvature terms cast into bracket form as well. Time stepping is performed using an explicit third order stiffly-stable scheme [23], with viscous terms treated implicitly using operator splitting. For more details on the numerical implementation see [24].

Nominal parameter values typical for tokamak edge plasmas are $\hat{\epsilon} = 18750$, $\hat{\mu} = 5$, $\hat{s} = 1$, $\omega_B = 0.05$ and $\mu_\Omega = \mu_n = 0.025$.

For parameter scans we varied $\hat{\beta}$ in a range between 0.1 – 30 and \hat{v} from 0.5 – 7.5. The scaling with $\hat{\beta}$ is especially interesting, as the drift-Alfvén system has the property that the nature of the turbulence changes with the degree to which the system is electromagnetic. This feature was demonstrated numerically by Scott [18] and Naulin [24] and also experimentally by Lechte *et al* [25]: The transition manifests itself in a change of the phase relationship between density and potential fluctuations, which varies for low values of k_y from a small phase angle in pure drift wave dynamics to $\pi/2$ in the MHD drift-ballooning regime. This is exemplified in Figure 1, which shows the phase probability distribution function as function of poloidal wavenumber for the cases $\hat{\beta} = 0.1$, $\hat{v} = 2.295$ and $\hat{\beta} = 30$, $\hat{v} = 0.5$. While in the low $\hat{\beta}$ case, the phase angle is always small, for the large $\hat{\beta}$ cases we observe a much broader phase relationship and a generally larger phase angle. The regime of dominating MHD ballooning instability is first reached at for the edge very high values of $\hat{\beta} > 30$ [24].

A time-trace of the kinetic energy, \mathcal{K} , of the fluctuating motions and the zonal flow energy $U = \int d\mathbf{x} (1/2) V_0^2$ is presented in Fig. 2. It is seen that while \mathcal{K} saturates after about 100 time units, the saturation of the flow takes place much later. Thus, all computations were run to times $t = 5000$, with time averages taken in the interval from time $t = 1000$ to the end of the simulation, to ensure a statistical steady state of fluctuating quantities. Moreover, from Figure 2 it is observed that the energy in the zonal flows is only a fraction of the total kinetic energy. This underlines the fact that no strong self-organized H-mode like transport barriers are formed in this system. However, zonal flows do form and influence the profile of transport as well as the density profile.

Due to the change in turbulence character connected to $\hat{\beta}$ we will now proceed and present in more detail two runs, the low beta $\hat{\beta} = 0.1, \hat{\nu} = 2.295$ and a high beta $\hat{\beta} = 30, \hat{\nu} = 0.5$ case.

Figure 3 shows a gray-scale plot of the zonal flow profile $V_0(x, t)$ and the zonal density $\langle n \rangle(x, t)$ in time, where in both cases we omit the damping layers in the plot. It is clearly seen that the zonal flows are radially localized and while exhibiting some fluctuation features, the flow profile is rather persistent in time. The zonal density shows some imprint of the zonal flow in terms of slightly elevated density levels in the vicinity of high flow shear, but fluctuations in the zonal density are more pronounced. It is worthwhile to remark that at about $t \approx 3750$ a weakening of zonal flows is clearly noticeable and prompts a transient radially propagating feature in the zonal density. This provides us a visualisation of the interplay between flows, transport and the density profile.

In Fig. 4 we present time traces of the energy transfer terms into the zonal flow and the rate of change of the zonal flow, together with the numerical error obtained by comparing the sum of the energy transfer terms with the computed actual change rate of the flow:

$$\delta F(t) = \frac{dV_0}{dt}_{Num.} - (\mathcal{R} + \mathcal{M} + \mathcal{G} + \mathcal{V}) . \quad (22)$$

Here $dV_0/dt_{Num.}$ is evaluated to second order in time [26]. The error $\delta F(t)$ is of the same order, and for $\hat{\beta} = 0.1$ the Maxwell stress energy transfer term \mathcal{M} , which is negligible for this low value of $\hat{\beta}$, when compared to each other energy transfer term, is of the same size. The statistical nature of the fluctuating flow drive terms is observed, as the balance between the transfer terms is only reached on a long time average, whereas on an instantaneous view the transfer terms can deviate significantly from their means. Here viscous damping \mathcal{V} and GAMs \mathcal{G} serve as sinks for the flow energy, which is solely driven by the Reynolds stress. While both damping terms vary on a rather slow time scale, the Reynolds stress and with it the resulting rate of the flow change vary on the faster time scale of the turbulence. Figure 5 shows correspondingly time traces of selected fluctuating quantities obtained at a single point and of flux surface averaged quantities at the same radial position. While the fluctuating quantities are all varying on the fast scale, the flux surface averaged ones vary significantly slower. Zonal density and zonal magnetic potential show, however, variations on a time scale of about 250 and 80 time units, respectively. The zonal flow V_0 shows some fast scale jitter, but varies only slowly over the shown 1500 time units. Thus, to investigate that time behavior in more detail we present in Fig. 6 the frequency spectra of flux surface averaged quantities connected to GAMs, as the density and the parallel ion velocity together with quantities related to zonal flow dynamics. The zonal density $\langle n \rangle$ and the

flux-surface averaged parallel ion velocity $\langle u \rangle$ show both a pronounced peak at a low frequency of about $\omega \approx 0.025$. This peak is clearly associated to the ideal geodesic oscillation around $\omega_{GAM} \approx \omega_B/\sqrt{2} = 0.035$. It is worthwhile to note that the GAM frequency arises by combining Eq. (12) with Eq. (20), and the ideal GAM frequency arises from the relation

$$\omega_B \langle \sin^2 z \frac{\partial \phi}{\partial x} \rangle = \frac{1}{2} \omega_B \langle [1 - \cos(2z)] \frac{\partial \phi}{\partial x} \rangle \approx \frac{1}{2} \omega_B V_0 \quad (23)$$

if the flux surface average of the term $(\cos(2z) \partial_x \phi)$ disappears exactly, as it would be expected for a fluctuations v_y being homogeneous along the parallel coordinate z . In toroidal geometry the $\phi(z)$ and thus $v_y(z) = \partial_x \phi$, however, show in general a distinct ballooning feature, resulting in higher amplitudes around position $z = 0$ than for $z = \pm\pi$. We thus expect the GAM peaks in the spectra to be shifted from the ideal ω_{GAM} , with the direction of the shift depending on the preferential direction of local flows v_y , and the width of the frequency shift depending on the ballooning properties of the velocity fluctuations $v_y(z)$. For our present parameters and a probe location one third into the radial x domain we experience a downshift by an additional factor of approximately $\sqrt{1/2}$.

For the zonal flow V_0 and the zonal vorticity, we observe that the zero frequency mode dominates the poloidal flow spectrum. At the frequency of the zonal density feature we observe even a small dip in the flow frequency spectrum, this supporting the observation that GAMs are a sink for the flow energy in that parameter regime.

For the high $\hat{\beta} = 30$ case the situation looks differently as is clearly seen from Fig. 7. The zonal flow profile is now broader and reveals much less persistence than in the low beta case (compare Fig. 3). Correspondingly the zonal density shows also a less pronounced radial structure and the characteristic time of the fluctuations seems to be of similar size for both zonal flow and zonal density profile.

The energy transfer rates \mathcal{R} , \mathcal{M} , and \mathcal{G} , shown in Fig. 8 reflect this change in behavior. We first observe that the Maxwell stress is now of finite size and a significant sink for the flow energy. It is very well correlated to the Reynolds stress in time, which still acts as a flow drive. For an ideal high beta MHD case in linear geometry without magnetic field curvature the balance between \mathcal{M} and \mathcal{R} is known to be exact with no preferred flow direction in the dynamics, as seen in Eq. (19). Here the resulting energy transfer from Maxwell and Reynolds stress is close to zero and the resulting change in the effective zonal flow drive is dominated by the GAMs \mathcal{G} , which now acts as a driving term. Consequently the resulting rate of change for the flow evolves mainly along with

the change in the GAM drive and shows only a minor additional variation on the timescale of the Reynolds and Maxwell stresses.

The time traces of fluctuating and averaged quantities shown in Fig. 9, reflect that behavior. We first note that the fluctuating quantities now show a somewhat more pronounced slower frequency, which reflects the frequency observed in the time evolution of the zonal quantities. All fluctuations are larger by about a factor three compared to the low beta $\hat{\beta} = 0.1$ case. The zonal density is up by a factor two to three and a slow oscillation is clearly observed in both the zonal density as the zonal magnetic potential. This slow frequency now is also found in the zonal flow time trace. These features get more obvious in the frequency spectra depicted in Fig. 10. A pronounced low frequency behavior is now seen also in the flow related quantities, namely in V_0 , which here exceeds the zero frequency component by about a factor two. In these situations the flow is not stationary (zero frequency) but is, compared to the turbulence, a slowly varying structure. The slow frequency of the flow is close to the ideal GAMs frequency ω_{GAM} , revealing the flow drive by this process. These results are generally in agreement with experimental observations, that show a modulation of the zonal flows at the frequency of the GAM oscillation [27, 30].

V. PLASMA BETA AND COLLISIONALITY SCALINGS

Here we present results concerned with the scaling of the different transfer terms with collisionality and plasma beta. In Fig. 11 we show the three main transfer terms as a function of $\hat{\beta}$ for a low collisionality of $\hat{\nu} = 0.5$. For increasing $\hat{\beta}$ the Reynolds stress drive \mathcal{R} gets slightly weaker, but is in all cases a drive. This indicates that the described flows do not decay through a Kelvin-Helmholtz like instability mechanism, which would make the Reynolds stress a sink term. The Maxwell stress \mathcal{M} starts close to zero and is always a sink term. It grows as expected in significance with increasing $\hat{\beta}$, and for large $\hat{\beta}$ is the dominating sink for the flow energy. The GAM transfer, \mathcal{G} , starts out as a sink for the flow energy at low beta, but with increasing beta it loses its importance as a sink. Finally, \mathcal{G} becomes positive for the high beta $\hat{\beta} = 30$ case, e. g. the GAM acts as a flow drive.

We then look at the scaling of flows and energy transfers with collisionality in the two cases of low and high beta. The results are presented in Fig. 12. We find that the saturation level of zonal flow energy decreases with rising $\hat{\nu}$ for low $\hat{\beta}$ and is in general by an order of magnitude smaller than the fluctuating kinetic energy $\mathcal{K} = \int d\mathbf{x} (1/2) (\nabla_{\perp} \tilde{\phi})^2$. The system is mainly gov-

erned by vortex dynamics [28], where the zonal flow contribution plays an important part for self-regulation of the fluctuation amplitudes, but is not dominating the energetics to an extent that it would completely suppress the turbulence. Further, we observe that the fluctuation energies \mathcal{K} and $\mathcal{P} = \int d\mathbf{x}(1/2)\tilde{n}^2$ and the turbulent particle transport $\Gamma_n = \int d\mathbf{x}v_x n$ both increase with parallel resistivity \hat{v} . This stronger turbulence level is due to the increasingly non-adiabatic nature of the electron response due to collisions, which increases the nonlinear drive of drift modes. The energy transfer terms behave as follows: The Reynolds stress decreases with increasing collisionality, accordingly with the decaying flow energy. The Maxwell stress energy transfer \mathcal{M} is always negligible at low beta and thus the flow energy is dissipated through the viscous terms \mathcal{V} and the geodesic channel.

Energies \mathcal{K} , \mathcal{P} and the transport Γ_n approximately double when changing to $\hat{\beta} = 30$ and taking the system from the drift into the ballooning regime. The magnetic flutter effect is then an important cause for the non-adiabatic response on the electrons. The influence of \hat{v} is accordingly much smaller and results in less variation for this high $\hat{\beta}$ case.

We observe that the Reynolds stress is always a drive ($\mathcal{R} > 0$) for the flow. At high beta the Maxwell stress is important and the balance between Maxwell and Reynolds stress becomes obvious as $|\mathcal{M}| \approx \mathcal{R}$ is reached and exceeded. Finally the electromagnetic flutter effect is taking out more energy from flows than is injected by Reynolds stress spin-up. The flow sustained in this high beta regime is now maintained by geodesic transfer *into* the flow. The driving effect by GAM oscillations on the flow is more pronounced for higher \hat{v} and higher levels of transport: GAM transfer is closely linked to the energy of density fluctuations in the $m = \pm 1$ sideband (and thus to energy in all other scales that couple by three-wave interaction to this sideband), which directly scales the transfer term \mathcal{G} . For higher resistivity the relative importance of \mathcal{G} is thus enhanced in the same amount as \tilde{n} increases both due to a more resistive as well as more electromagnetic electron response. The strong magnetic flutter \tilde{B}_\perp in high beta turbulence can cause significant chaotic deviations of field lines radially and poloidally from the flux coordinates that were defined for an unperturbed magnetic field. The parallel coupling is thus able to connect regions of neighboring radial domains where the amount of radial overlap is rising with $\hat{\beta}$. Zonal structures may be efficiently destroyed for a strong flutter effect, and the aligning character of Reynolds stress on zonal flows is counteracted, thus also the radial structure of the zonal flows is less pronounced in the high beta case, see Fig. 7. The drive of vortices on the drift wave scales is of course still maintained by the free energy in the background density gradient, and the energy

on drift scale density fluctuations is even increased by the destabilising magnetic flutter effect on the non-adiabatic parallel dynamics. The cascade in density structures is generally a three-wave interaction that is on statistical grounds essentially down to smaller scales, but is by more infrequent events also able to feed scales in the $m = \pm 1$ geodesic sidebands and the $m = 0$ zonal mode. The geodesic transfer pathway is thus open in both directions: a strong drive of the GAM mode by zonal flows for low beta on the average drains energy out of the flow to smaller scales. For high beta the GAM energy is, however, converted to a certain extent into $\tilde{\phi}$ oscillations that supply the zonal flows.

VI. CONCLUSION

We have performed a detailed investigation of the zonal flow drive in drift-Alfvén turbulence for parameters relevant to the edge region of hot plasmas in toroidal devices. We have identified three main mechanisms for the interaction of the zonal flows with the turbulent fluctuations; namely the electrostatic Reynolds stress, the electromagnetic Maxwell stress, and the geodesic acoustic mode, GAM, coupling. The main results are summarized as follows: For low beta cases the Maxwell stress is negligible and the Reynolds stress is the only driving term of the flow, whereas the GAM coupling provides a sink for the flow in addition to the viscosity. For the case of high-beta plasmas, however, the Maxwell stress becomes significant. It acts as a sink for all the cases we have investigated, and it efficiently cancels the driving effect of the Reynolds stress. In this parameter regime the flow is mainly sustained by the GAM coupling, that now acts as a drive opposing the viscous damping.

We should therefore emphasize that from an experimental point of view, measuring Reynolds stress exclusively as an indication for flow generation is in general not sufficient. The electromagnetic Maxwell stress is important already at a moderate edge beta parameter, and will be even more important for ITER like plasmas with higher edge β at reduced collisionality. This clearly opens a demand for additional measurements of the Maxwell stress.

There is a clear trend in the computational results that assign more importance to the GAM oscillation at a high level of transport. The GAMs present a driving mechanism for the flows if the transport is sufficiently inhomogeneous: with an increasing ballooning character of the turbulence the GAMs are further excited and can ultimately drive flows.

The frequency spectra of the zonal flow clearly show a dip or a peak in the ω_{GAM} frequency

range, depending on the sink or drive role of the GAMs for the flow evolution. Measurements of the frequency spectrum of the zonal flow should thus be able to distinguish between these two scenarios and provide further insight into the importance of GAMs for the flow, and finally for H-mode formation.

Finally we note that our numerical results are for the high beta case partially in disagreement with recent results by B. Scott [11] regarding the specific role of the Maxwell stress [29].

Acknowledgments

This work was supported by the Danish Center for Scientific Computing (DCSC), grants CPU-1101-08 and CPU-1002-17.

-
- [1] F. Wagner *et al.*, Phys. Rev. Lett. **49**, 1408 (1982).
- [2] J. W. Connor and H. R. Wilson, Plasma Phys. Controlled Fusion **42**, R1 (2000).
- [3] J. Hugill, Plasma Phys. Controlled Fusion **42**, R75 (2000).
- [4] P. W. Terry, Rev. Mod. Phys. **72**, 109 (2000).
- [5] A. Hasegawa and M. Wakatani, Phys. Rev. Lett. **59**, 1581 (1987).
- [6] C. Hidalgo *et al.*, Phys. Rev. Lett. **91**, 065001 (2003).
- [7] V. Antoni *et al.*, in *20th IAEA Fusion Energy Conference*, IAEA (IAEA, Vienna, 2004), pp. EX/8–4Ra.
- [8] R.-H. Lu *et al.*, Phys. Lett. A **333**, 298 (2004).
- [9] N. Winsor, J. L. Johnson, and J. M. Dawson, Phys. Fluids **11**, 2448 (1968).
- [10] K. Hallatschek and D. Biskamp, Phys. Rev. Lett. **86**, 1223 (2001).
- [11] B. D. Scott, Phys. Lett. A **320**, 53 (2003).
- [12] M. Wakatani, M. Sato, N. Miyato, and S. Hamaguchi, Nucl. Fusion **43**, 63 (2003).
- [13] E. J. Kim, T. S. Hahm, and P. H. Diamond, Phys. Plasmas **8**, 3576 (2001).
- [14] B. D. Scott, Plasma Phys. Control. Fusion **39**, 1635 (1997).
- [15] B. D. Scott, Phys. Fluids B **4**, 2468 (1992).
- [16] S. I. Braginskii, in *Reviews of Plasma Physics*, edited by M. A. Leontovich (Consultants Bureau, New York, 1965).
- [17] N. Bian and O. Garcia, Phys. Plasmas **10**, 4696 (2003).
- [18] B. D. Scott, Plasma Phys. Control. Fusion **39**, 471 (1997).
- [19] A. B. Hassam and J. F. Drake, Phys. Fluids B **5**, 4022 (1993).
- [20] P. N. Guzdar *et al.*, Phys. Fluids B **5**, 3712 (1993).
- [21] T. E. Stringer, Phys. Rev. Lett. **22**, 770 (1969).
- [22] A. Arakawa, J. Comput. Phys. **1**, 119 (1966).
- [23] G. E. Karniadakis, M. Israeli, and S. A. Orszag, J. Comput. Phys. **97**, 414 (1991).
- [24] V. Naulin, Phys. Plasmas **10**, 4016 (2003).
- [25] C. Lechte, S. Niedner, and U. Stroth, New J. Phys. **4**, Art. No. 34 (2002).
- [26] V. Naulin and A. H. Nielsen, SIAM Journal on Scientific Computing **25**, 104 (2003).
- [27] G. R. McKee *et al.*, Phys. Plasmas **10**, 1712 (2003).
- [28] V. Naulin, O. E. Garcia, A. H. Nielsen, and J. Juul Rasmussen, Phys. Letters A **321**, 355 (2004).

[29] B. D. Scott, submitted to New J. Phys., (2005).

[30] G.D. Conway, B.D. Scott, J. Schirmer, M. Reich, A. Kendl and the ASDEX Upgrade Team, Proc. 31st EPS Conference on Plasma Physics (28.6.- 2.7.2004, London).

Figures

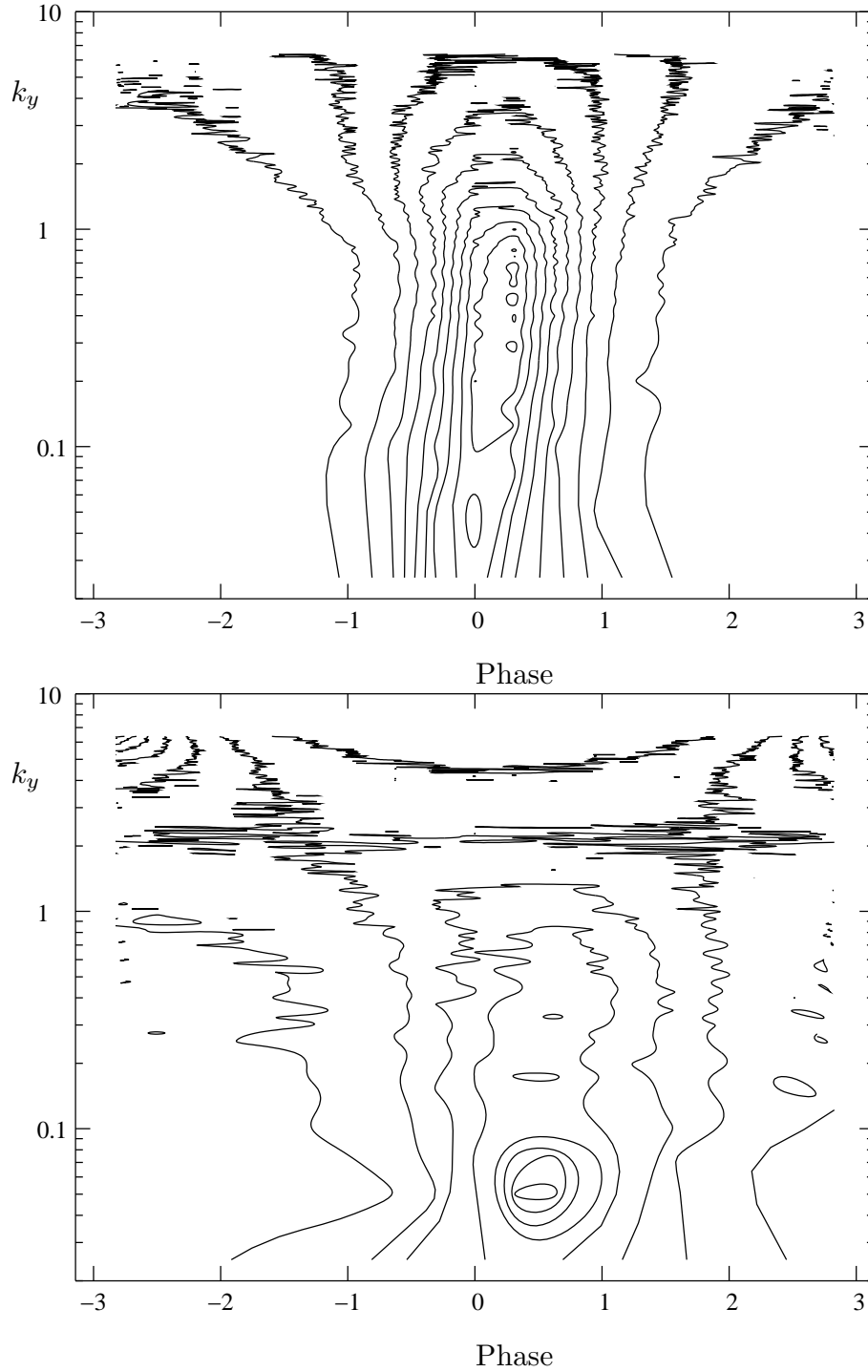


FIG. 1: Phase angle probability between density and potential fluctuations for the low $\hat{\beta} = 0.1$ (top) and high $\hat{\beta} = 30$ (bottom) case.

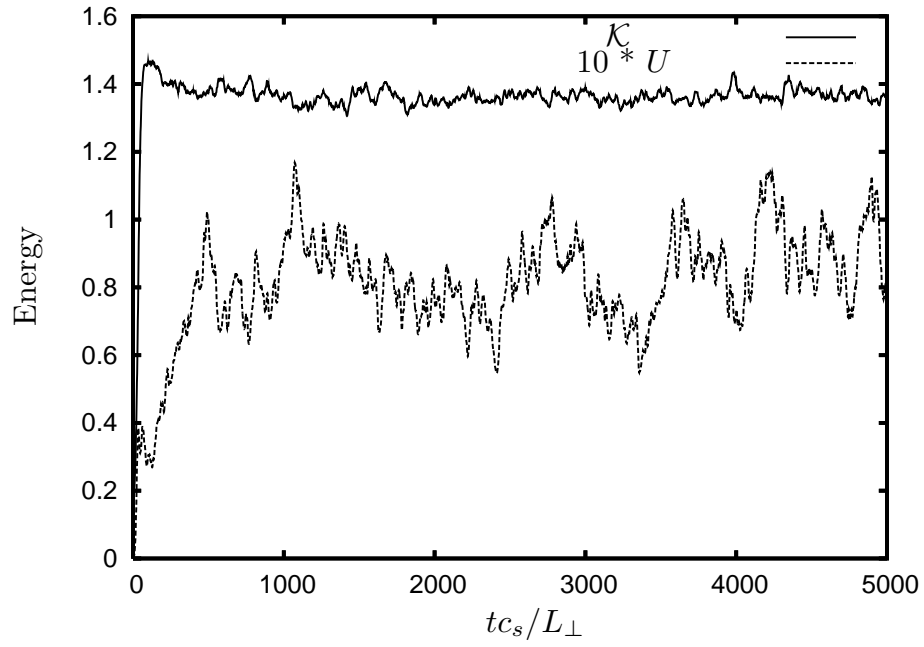


FIG. 2: Kinetic energy \mathcal{K} and energy in zonal-flow component U over time for the low $\hat{\beta} = 0.1$ case.

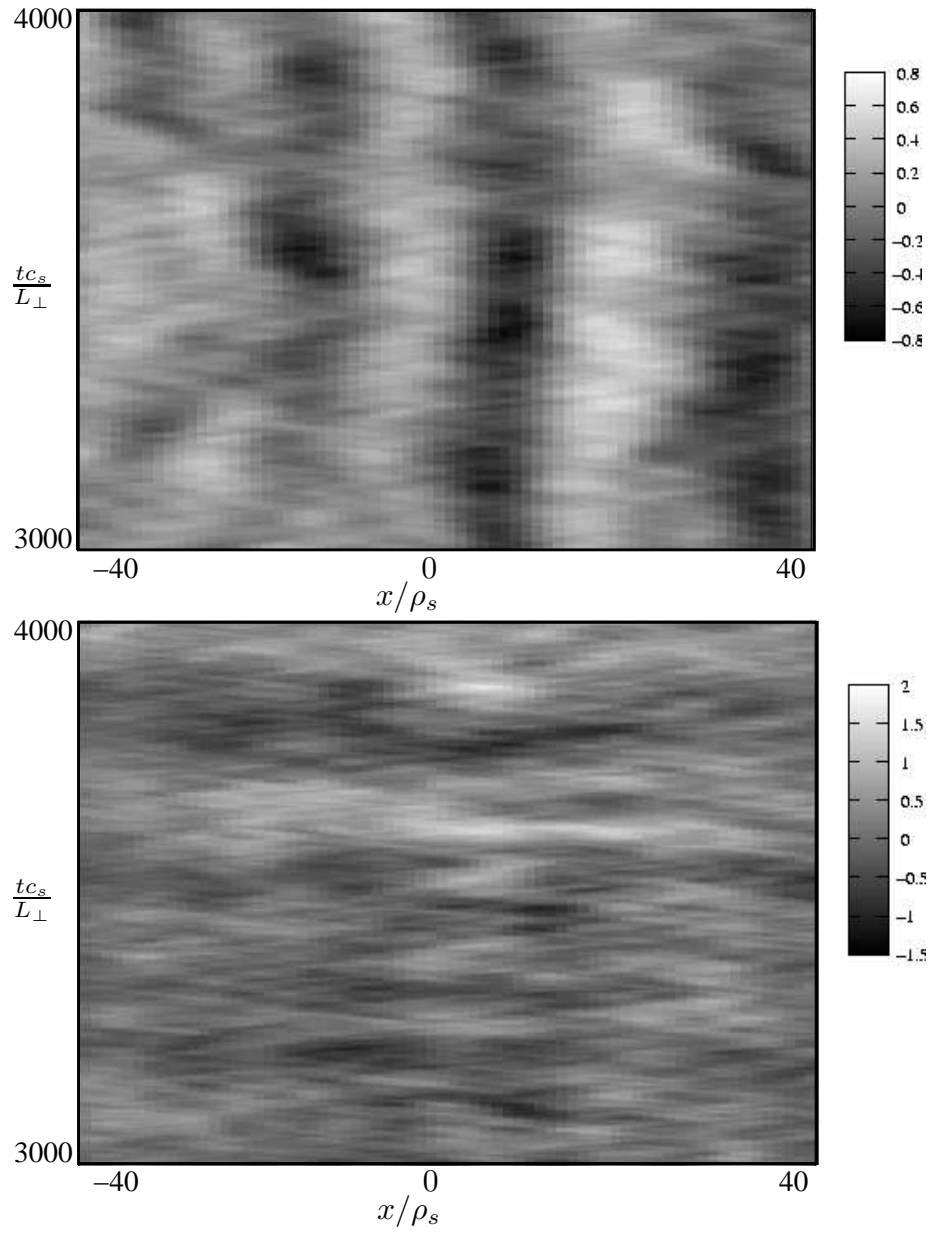


FIG. 3: Space-time evolution of zonal flow $V_0(x,t)$ (top) and zonal density $\langle n \rangle(x,t)$ (bottom) for $\hat{\beta} = 0.1$.

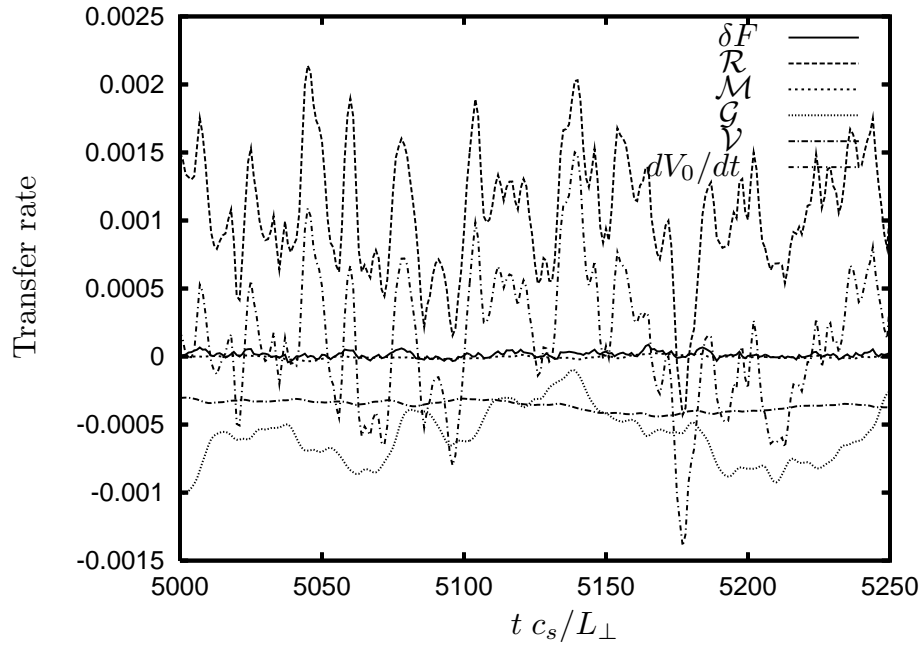


FIG. 4: Energy exchange terms, flow change rate, and numerical error for $\hat{\beta} = 0.1$. Reynolds stress is the key drive and GAMs are acting as a sink for the flow energy.

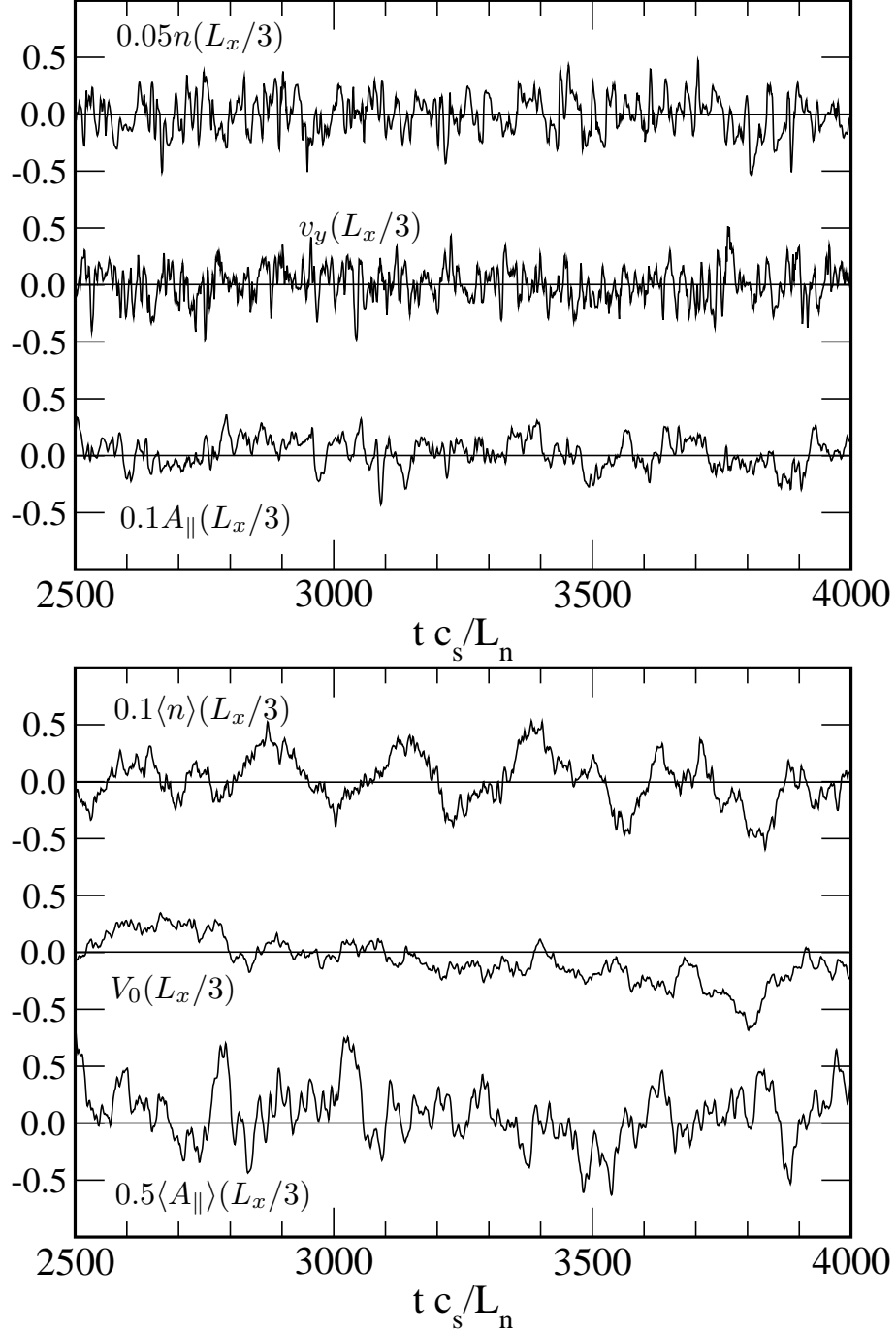


FIG. 5: Fluctuating quantities (top) and fluxsurface averaged quantities (bottom) for $\hat{\beta} = 0.1$, measured at $x = L_x/3$ and on the outboard midplane.

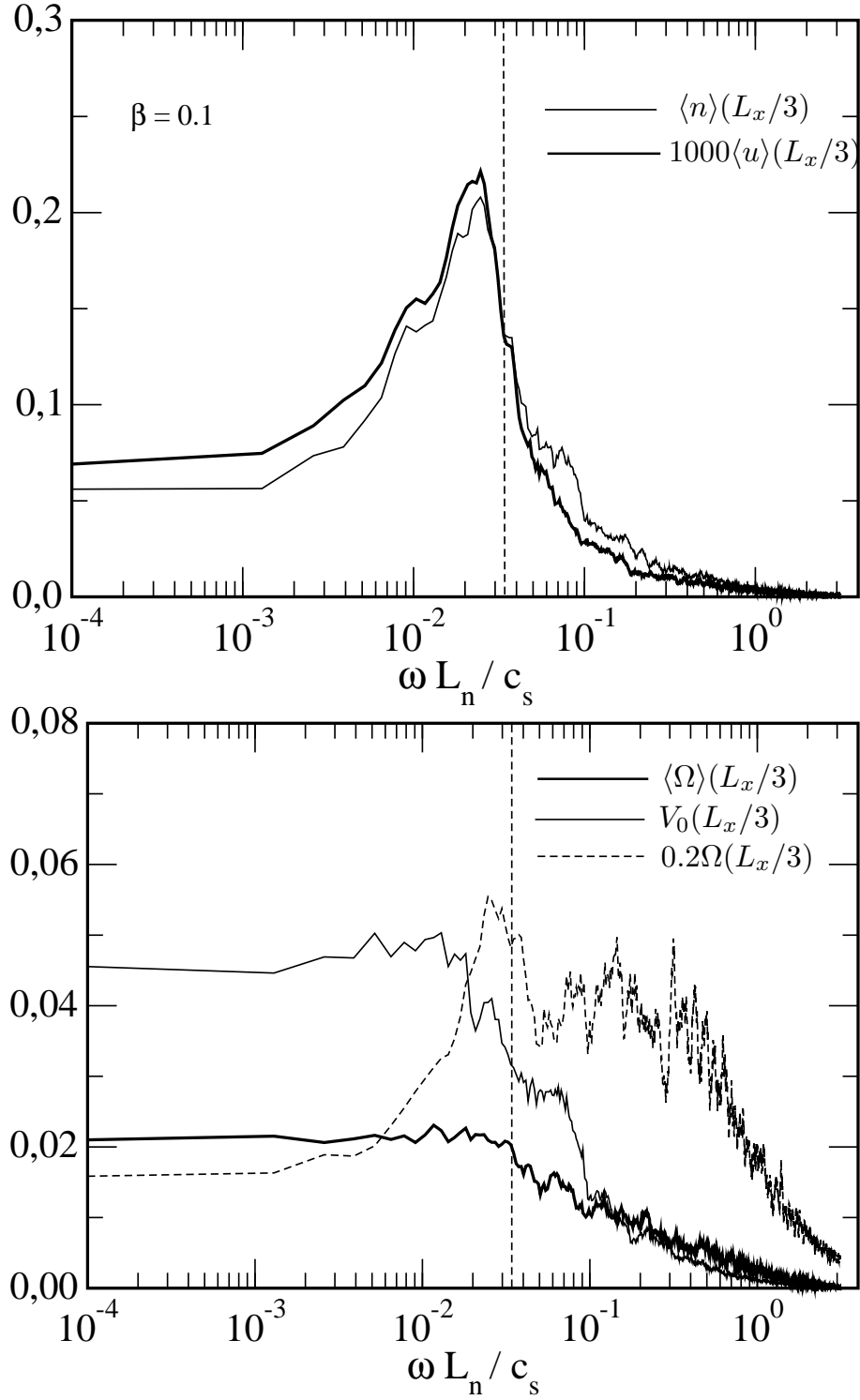


FIG. 6: Frequency spectra of quantities associated with GAM oscillation (top) and flows (bottom) for $\hat{\beta} = 0.1$. The vertical line indicates the ideal GAM frequency ω_{GAM} .

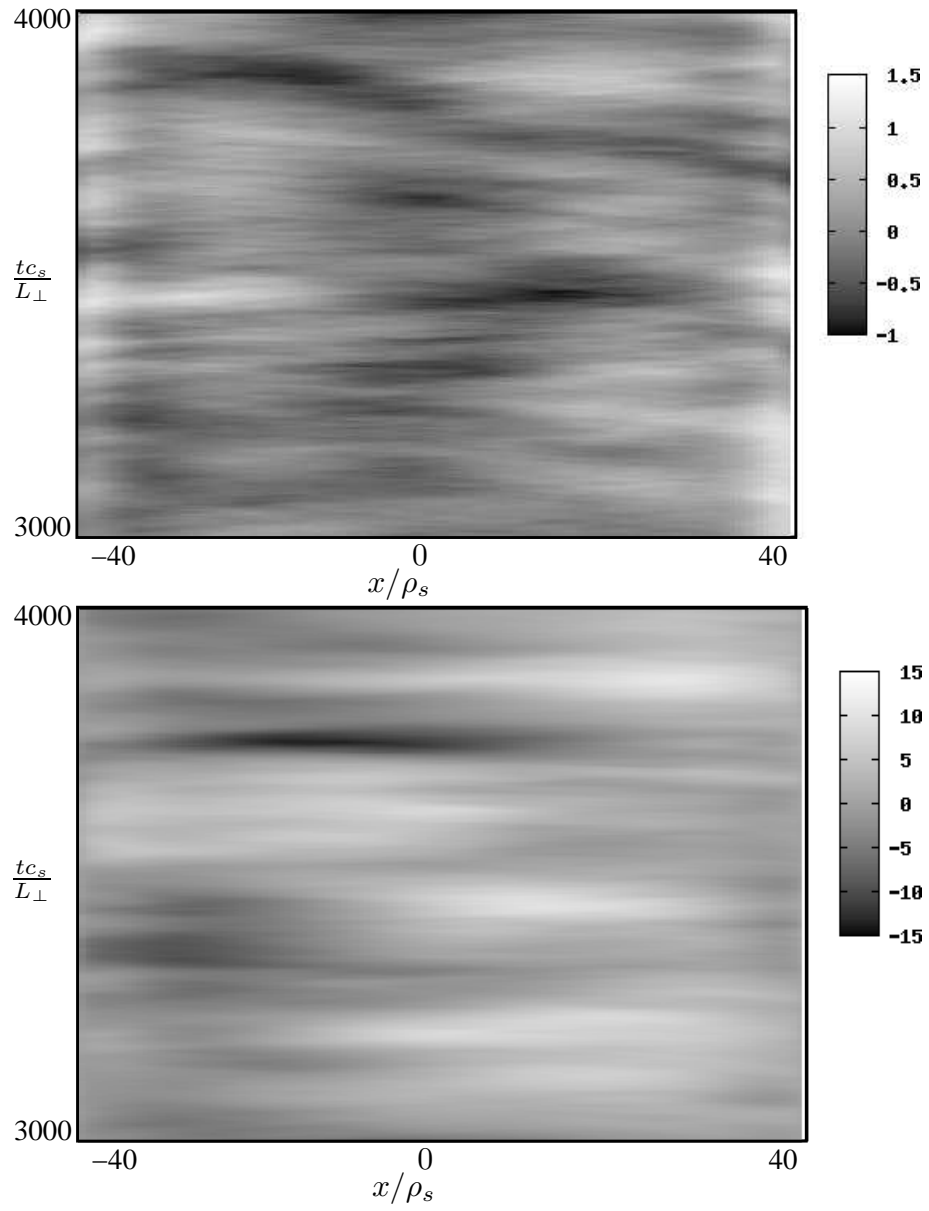


FIG. 7: Space-time evolution of zonal flow $V_0(x,t)$ (top) and zonal density $\langle n \rangle(x,t)$ (bottom) for $\hat{\beta} = 30$.

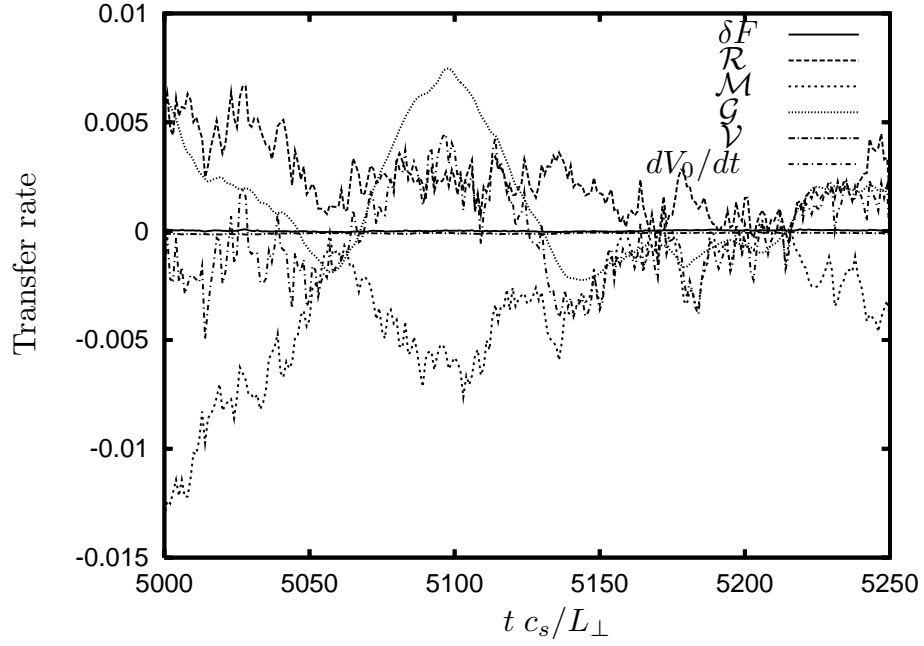


FIG. 8: Energy exchange terms, flow change rate, and numerical error for $\hat{\beta} = 30$, showing the dominating influence of the GAMs for flow drive in that regime.

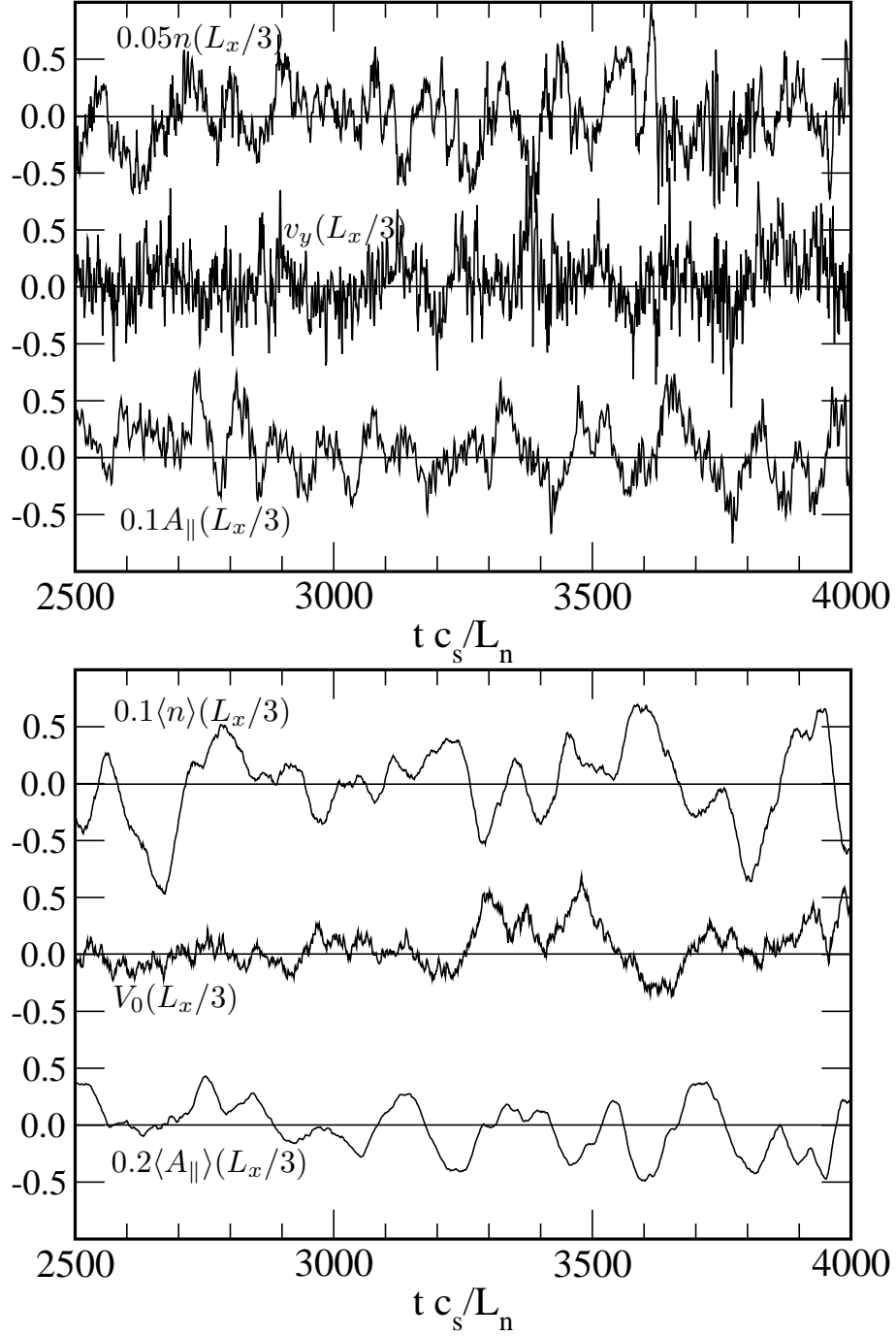


FIG. 9: Fluctuating quantities and fluxsurface averaged quantities for $\hat{\beta} = 30$, measured at $x = L_x/3$ and on the outboard midplane.

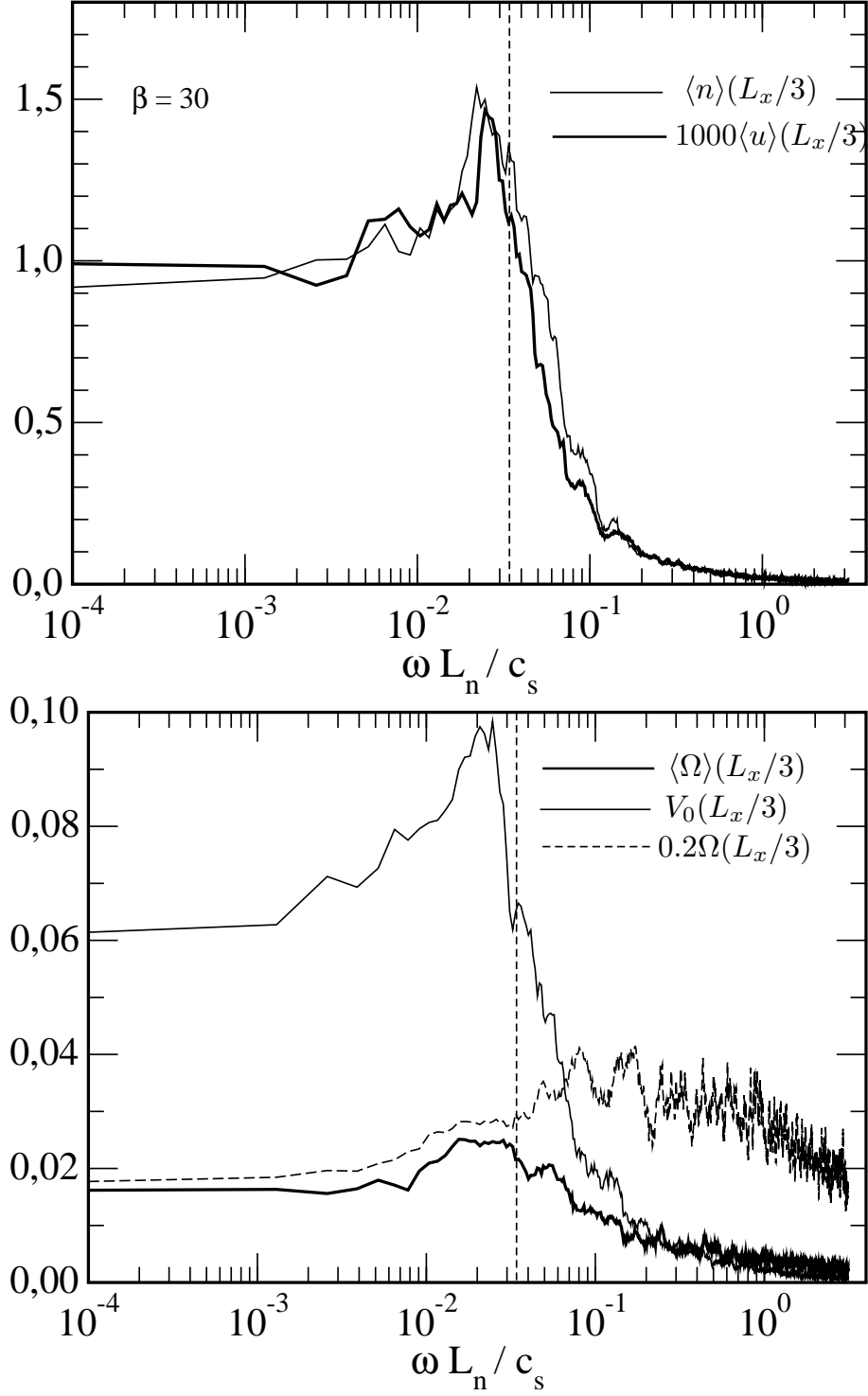


FIG. 10: Frequency spectra of quantities associated with GAM oscillation (top) and flows (bottom) for $\hat{\beta} = 30$. The vertical line indicates the ideal GAM frequency ω_{GAM} .

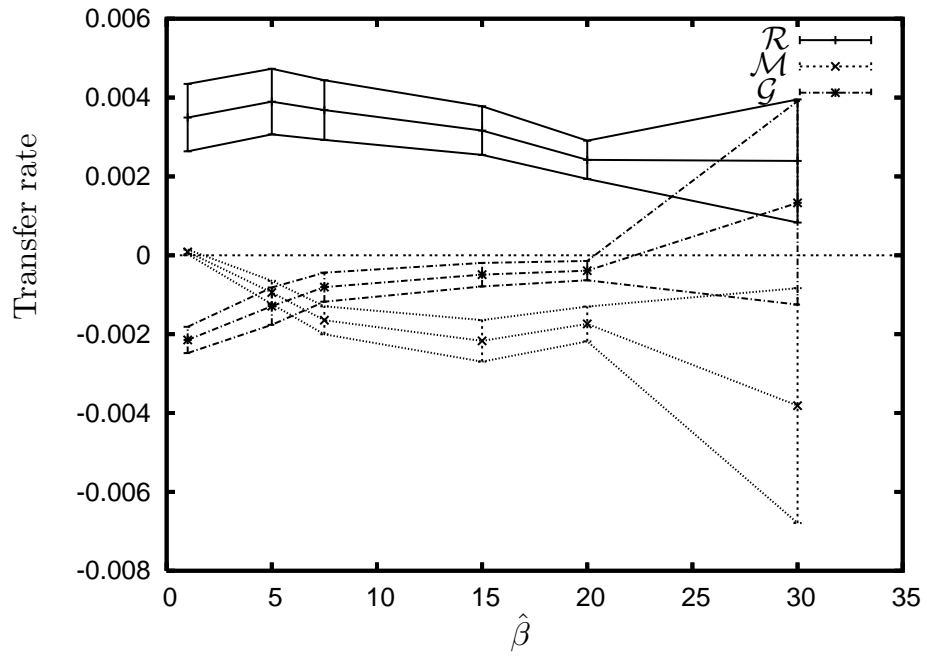


FIG. 11: Dependence of flow energy transfer terms terms on $\hat{\beta}$ for $\hat{v} = 0.5$, with standard deviation.

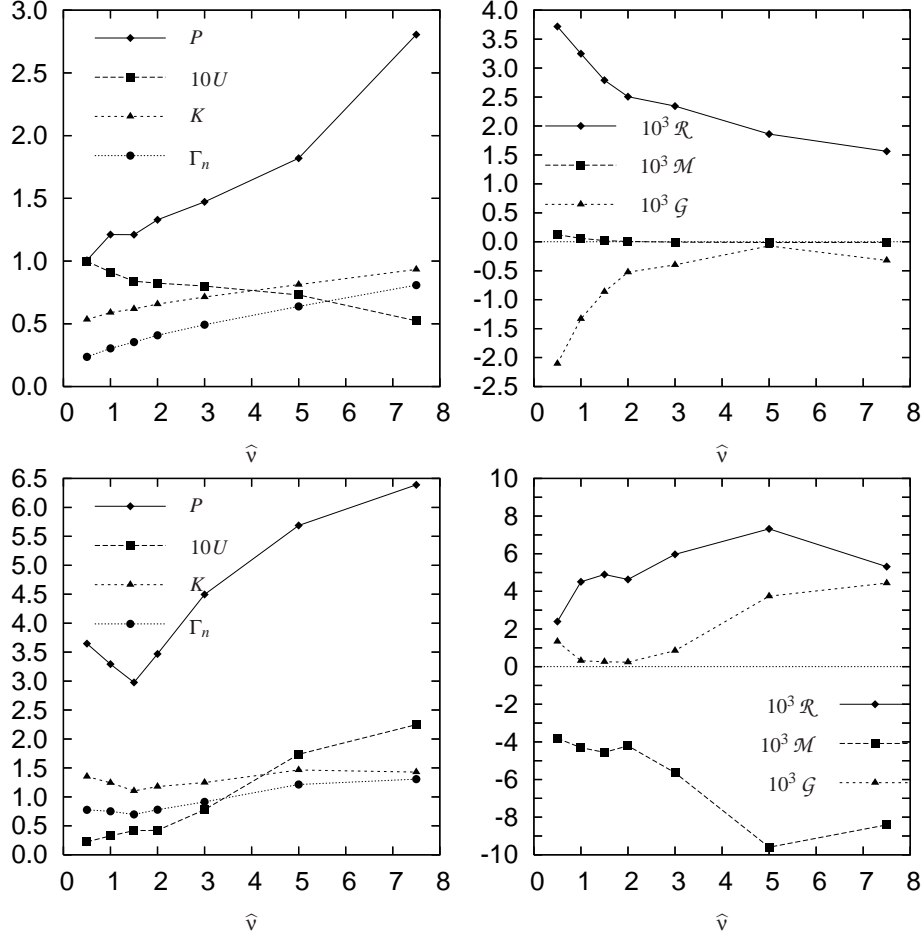


FIG. 12: Scan over collisionality \hat{v} for low $\hat{\beta} = 1.0$ (top) and high $\hat{\beta} = 30$ (bottom). The left side shows energy in the density fluctuations P , kinetic energy K , flow energy U and particle flux Γ_n . The right side depicts energy transfer terms.